Ultrasound multifrequency strategy to estimate the lung surface roughness, *in silico* and *in vitro* results

Federico Mento [a], Matteo Perini [b], Ciro Malacarne [b], Libertario Demi [a],*

[a] *Department of Information Engineering and Computer Science, University of Trento, Via Sommarive 9, 38123 Trento, Italy*
[b] *Polo Meccatronica (ProM), Via Fortunato Zeni 8, 38068 Rovereto, Italy*

A R T I C L E   I N F O

A B S T R A C T

Lung ultrasound (LUS) is an important imaging modality to assess the state of the lung surface. Nevertheless, LUS is limited to the visual evaluation of imaging artifacts, especially the vertical ones. These artifacts are observed in pathologies characterized by a reduction of dimensions of air-spaces (alveoli). In contrast, there exist pathologies, such as chronic obstructive pulmonary disease (COPD), in which an enlargement of air-spaces can occur, which causes the lung surface to behave essentially as a perfect reflector, thus not allowing ultrasound penetration. This characteristic high reflectivity could be exploited to characterize the lung surface. Specifically, air-spaces of different sizes could cause the lung surface to have a different roughness, whose estimation could provide a way to assess the state of the lung surface. In this study, we present a quantitative multifrequency approach aiming at estimating the lung surface's roughness by measuring image intensity variations along the lung surface as a function of frequency. This approach was tested both *in silico* and *in vitro*, and it showed promising results. For the *in vitro* experiments, radiofrequency (RF) data were acquired from a novel experimental model. The results showed consistency between *in silico* and *in vitro* experiments.

1. Introduction

Lung ultrasound (LUS) is nowadays widely adopted in clinical practice to assess the state of the lung surface [1,2]. Specifically, the main characteristics of LUS (i.e., portability, real-time imaging, and non-ionizing radiations) render it particularly suitable for patients' monitoring [3,4].

Nevertheless, being LUS mainly based on the visual evaluation of imaging artifacts, it remains subjective and qualitative [1,2,4,5]. To improve LUS specificity, researchers have recently started to develop quantitative LUS approaches aiming at estimating the state of the lung surface [6-13]. However, these approaches can be used to assess the state of lung surface only in pathologies characterized by a reduction of dimensions of air-spaces (alveoli), and thus an increased permeability of the lung with respect to ultrasound waves [2,14]. Therefore, these techniques cannot be used for patients affected by lung pathologies characterized by an enlargement of air-spaces [14].

Being the third leading cause of death worldwide (causing 3.23 million deaths in 2019) [15,16], chronic obstructive pulmonary disease (COPD) can be considered the most representative example of lung disease characterized by an enlargement of air spaces. Indeed, the

peripheral air-space dimensions in COPD patients are generally above 490 µm, whereas they are mainly between 340 and 440 µm in healthy subjects [17]. Similarly to what happens in a healthy lung, the enlargement of peripheral air-spaces' dimensions causes the lung surface to behave essentially as a perfect reflector, thus not allowing ultrasound penetration [14]. This characteristic high reflectivity could be exploited to characterize the lung surface. Specifically, we hypothesize that air-spaces of different sizes could cause the lung surface to exhibit a different roughness [18], whose estimation could provide a way to assess the state of the lung surface [14]. To clarify, as the increase of air-spaces' dimensions can occur also peripherally (thus, at the lung surface) [17,18], this increase is implicitly translated into a variation of lung surface (air) roughness. Fig. 1 shows a pictorial representation of lung surface roughness variation following air-spaces' enlargement. This enlargement of peripheral air-spaces causing the lung surface to have a different roughness can be clearly observed from lung histologies of COPD patients, as shown in [18].

In this study, we present a quantitative multifrequency approach aiming at estimating the lung surface's roughness. In particular, this estimation is performed by measuring image intensity variations along the lung surface as a function of frequency [14]. Specifically, when
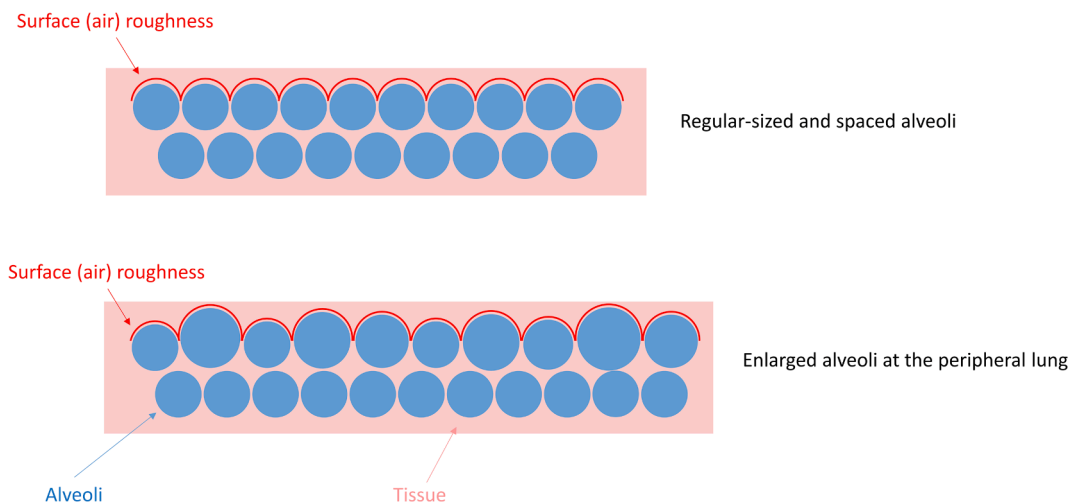

Fig. 1. Pictorial representation of lung surface roughness variation following air-spaces' enlargement. The top representation shows regular-sized and spaced alveoli (air-spaces), whereas the bottom representation shows the disposition of enlarged alveoli (air-spaces) at the peripheral lung. The alveoli are represented in light blue, the surface roughness is represented as a red line, and tissue is represented in pink. (For interpretation of the references to colour in this figure legend, the reader is referred to the web version of this article.)
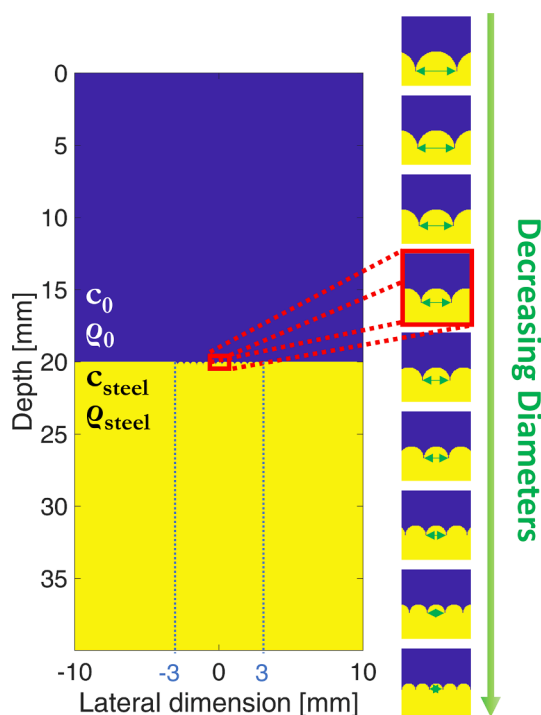

Fig. 2. The simulated computational domain is shown. The first 20 mm of depth consist of muscle (blue). A simulated lung surface, consisting of steel (yellow), was added at 20 mm. This surface has different roughness levels, modeled with semi-circular scatterers (representing alveoli), which have a diameter ranging from 200 to 600 μm, with a 50-μm step-size (between −3 to 3 mm in lateral dimension). The figure shows an example of domain with scatterers' diameter equal to 450 μm (left). The same area of the domain is shown for all the levels of roughness (right). (For interpretation of the references to colour in this figure legend, the reader is referred to the web version of this article.)

roughness is introduced at the surface and a wave is transmitted in a direction perpendicular to the surface, it is expected that a part of the wave is back-scattered in directions different from the transmitted one, thus causing a decrease of intensity. This deviation from the transmission direction should depend on the relation between the wavelength

(thus, the frequency) in the propagation medium (i.e., soft tissues) and the roughness. Therefore, we aim at understanding whether it is possible to observe intensity variations of the waves back-scattered from a rough surface, map this variation, and, finally, evaluate the possibility to extract information on the roughness dimensions from the obtained map. We set our experiments in specific ranges of roughness and frequency, which correspond to the range of interest of peripheral air-spaces' dimensions [17] and the frequencies typically used in medical ultrasound, respectively. This approach was tested both *in silico* (numerical simulations), and *in vitro*, where radiofrequency (RF) data were acquired from a novel experimental model.

The paper is organized as follows. While materials and data acquisition are presented in Sec. 2.1, the process to quantify the surface intensity is described in Sec. 2.2. The results are then presented in Sec. 3, followed by discussion and conclusions in Sec. 4.

2. Materials and methods

2.1. Materials and data acquisition

2.1.1. In silico

The computational 2D (two-dimensional) domain simulated with the k-wave [19] MATLAB toolbox consisted of 2000×4000 pixels along the lateral dimension and depth, respectively. As the numerical grid-size (square pixels) was equal to 10 μm, the physical size of computational domain resulted in 20×40 mm. Specifically, a homogeneous muscle layer was simulated in the first 20 mm of depth, whereas a lung surface with 9 different levels of roughness was added at 20 mm [14]. The roughness was simulated by introducing, at the lung surface, semi-circular scatterers (representing alveoli) having a diameter ranging from 200 to 600 μm, with a 50-μm step-size. This roughness was introduced only in the central part of the domain (between −3 and 3 mm in the lateral dimension), whereas the remaining parts of the interface (from −10 to −3 mm and from 3 to 10 mm) were kept smooth (see Fig. 2). This was done to clearly visualize intensity variations between the smooth and the rough parts of the mimicked lung surface. Moreover, the smooth areas served as reference points when the reconstructed images were normalized with respect to their maximum (see Sec. 2.2).

Steel was used to mimic the lung surface, as it can simulate a highly reflective acoustic interface. Specifically, the reflection coefficient of a steel/muscle interface ($R \cong 0.93$) is comparable with the reflection coefficient of an air/muscle interface ($R \cong 0.99$). It is important to

Table 1
Simulated acoustic properties for muscle and steel.

Medium	Speed of sound [m/s]	Volumetric mass density [kg/m^3]	Acoustic impedance [MRayl]
Muscle [22]	$c_0 = 1580$	$\rho_0 = 1041$	$Z_0 = c_0 \times \rho_0 \cong 1.645$
Steel [23]	$c_{steel} = 5940$	$\rho_{steel} = 7860$	$Z_{steel} = c_{steel} \times \rho_{steel} \cong 46.69$

Table 2
Wavelength values for muscle and steel and their ratio with the numerical grid-size.

	Frequency [MHz]							
	3	4	5	6	7	8	9	10
λ_0 [μm]	527	395	316	263	226	198	176	158
λ_0/grid-size	52.7	39.5	31.6	26.3	22.6	19.8	17.6	15.8
λ_{steel} [μm]	1980	1485	1188	990	849	743	660	594
λ_{steel}/grid-size	198	148.5	118.8	99	84.9	74.3	66	59.4

highlight how a material able to form a highly reflective acoustic interface is needed as we aim at analyzing the phenomena occurring at the interface and not inside that material. Moreover, steel allowed us to fabricate lung-mimicking phantoms having controllable size at micrometric scale, thus providing us the possibility for a consistent comparison with the *in silico* experiments. Table 1 shows the simulated acoustic properties for muscle and steel.

For each domain, data were acquired with a plane wave imaging strategy by transmitting a 4-μs-time-length pulse (bandwidth equal to 0.5 MHz at −6 dB), and center frequencies from 3 to 10 MHz, with a 1-MHz step size (8 images per domain). Table 2 shows the wavelength values for muscle (λ_0) and steel (λ_{steel}), as well as their ratio with the numerical grid-size. In transmission phase, the entire array (composed by 64 elements) was excited. The kerf and pitch were 45 and 245 μm, respectively; however, for the domain approximation, the actual simulated values were 40 and 240 μm, respectively. The array was placed at 150 μm of depth from the beginning of the computational domain, and centered with respect to the lateral dimension (i.e., laterally extending from approximately −7.7 mm to 7.7 mm). To reconstruct each image, a sub-array of 16 elements was linearly shifted along the entire array in reception, thus forming images composed by 49 lines along the lateral dimension. No focus was applied both in transmission and reception

phases. The time sampling interval dt equals to 316 ps, resulting in a sampling frequency of 1/dt ≅ 3.1645 GHz. No time gain compensation (TGC) was applied, and a speed of sound of 1580 m/s was assumed for the time–space conversion (along depth).

The choice of a plane wave imaging strategy was made to save computational time (thus, performing a higher amount of simulations). Similarly, plane wave transmissions were used *in vitro*.

2.1.2. In vitro

The ULA-OP programmable platform [20] and an LA533 (Esaote, Florence, Italy) linear array probe (having pitch and element size along the lateral dimension equal to 245 and 220 μm, respectively [21]) were exploited to acquire RF data with different center frequencies. Specifically, the data were acquired by transmitting pulses having the same bandwidth and center frequency of the *in silico* experiments. The utilized probe has a −6 dB bandwidth from 3.8 to 12 MHz and a −12 dB bandwidth from 3.2 to 13.2 MHz [11]. The maximum of the transducer transfer function is at 8 MHz. A 50 MHz sampling frequency was used (dt = 20 ns). A sub-aperture of 64 elements was employed in transmission and reception, and the images were reconstructed with dynamic beamforming (dynamic focus in reception). Each final image, which was reconstructed by linearly shifting this sub-aperture over the entire array (192 elements), consists of 129 lines. To avoid saturation phenomena, the driving signal amplitude was maintained to 10% of the maximum amplitude allowed by the ULA-OP system [12]. To clarify, the driving signal is the electrical signal utilized to excite each element of the transmit aperture (the maximum output voltage is 24 Vpp [20]). No time gain compensation (TGC) was applied, and a speed of sound of 1480 m/s was assumed for the time–space conversion (along depth).

To *in vitro* mimic the same levels of roughness utilized *in silico*, a phantom consisting of austenitic stainless steel AISI (American Iron and Steel Institute) 316L (Euronorm number = 1.4404) was produced by a Concept Laser Mlab (General Electric Additive, Boston, US), i.e., a 3D metal LPBF (laser powder bed fusion) printer (maximum power = 100 Watts, and laser spot size = 45 μm). Specifically, the phantom consisted of 9 stripes along its length made with varying roughness. Each rough stripe was composed of semi-cylinders arranged consecutively along the phantom width. The 9 rough stripes were separated by 8 smooth stripes (no roughness), each having the same length (1 cm). Therefore, as shown in Fig. 3, the total phantom length was 17 cm (9 cm + 8 cm), whereas its width was 5 cm (to allow the probe to laterally cover the entire area).

The steel phantom was immersed in a water tank and positioned on a steel plate (Fig. 4), which was used to align the phantom consistently
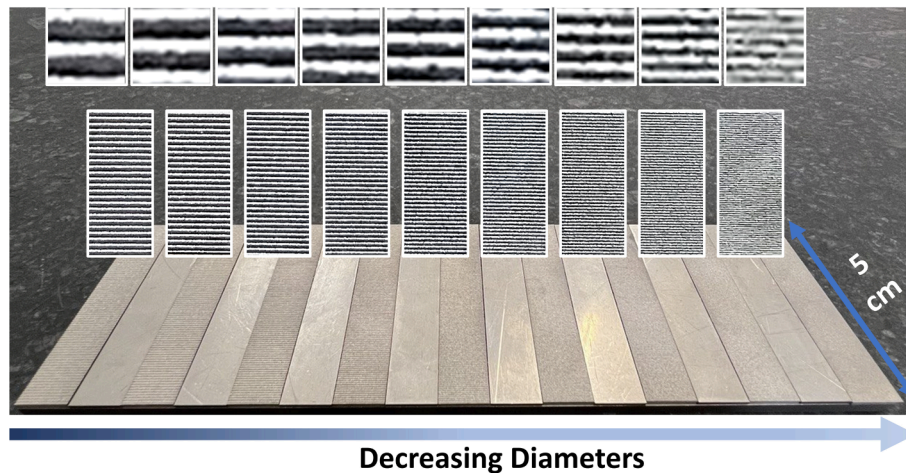

Fig. 3. Picture of the steel model is shown. The model has a width of 5 cm to allow the probe to laterally cover the entire area. The length of each rough stripe is 1 cm, for a total of 17 cm (9 levels of roughness + 8 smooth areas to separate the different levels of roughness). The figure shows zoomed areas for each rough stripe (center). An additional zoom operation shows the finer details of each rough stripe (top).
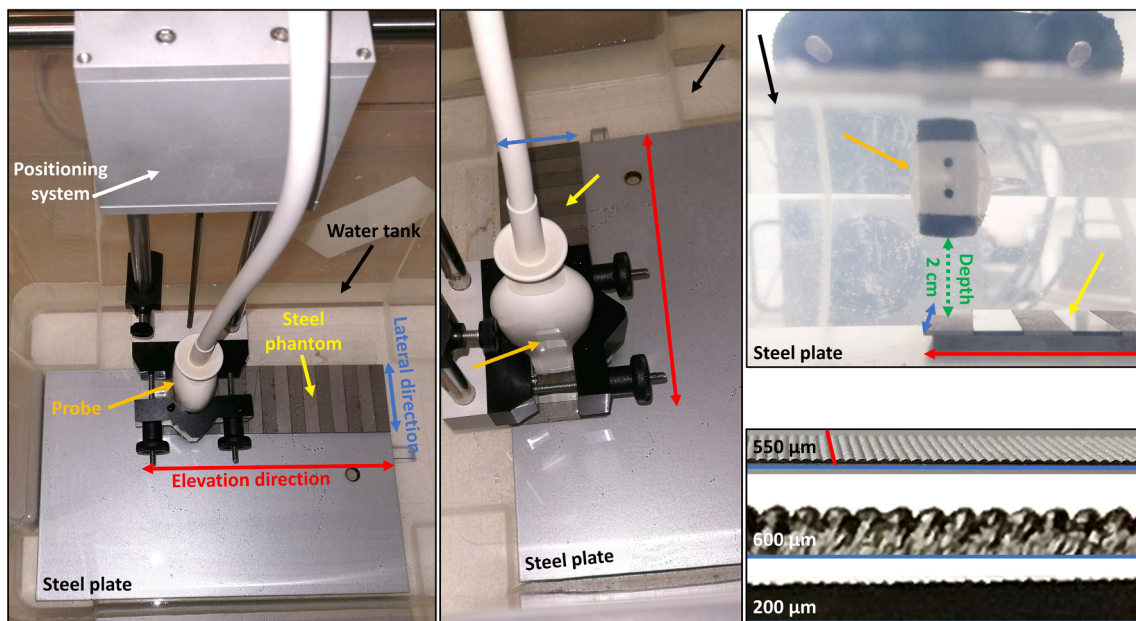
Fig. 4. The utilized steel phantom (yellow), probe (orange), positioning system (white), steel plate, water tank (black), and the three directions, i.e., lateral (blue), elevation (red), and depth (dashed green), are shown. Three pictures (left, center, and top right) show the geometry of the acquisition from three different views. The distance between the phantom and the probe is approximately equal to 2 cm (top right). The bottom right pictures show the finer details of different rough stripes of the steel phantom (550 μm, 600 μm, and 200 μm). (For interpretation of the references to colour in this figure legend, the reader is referred to the web version of this article.)
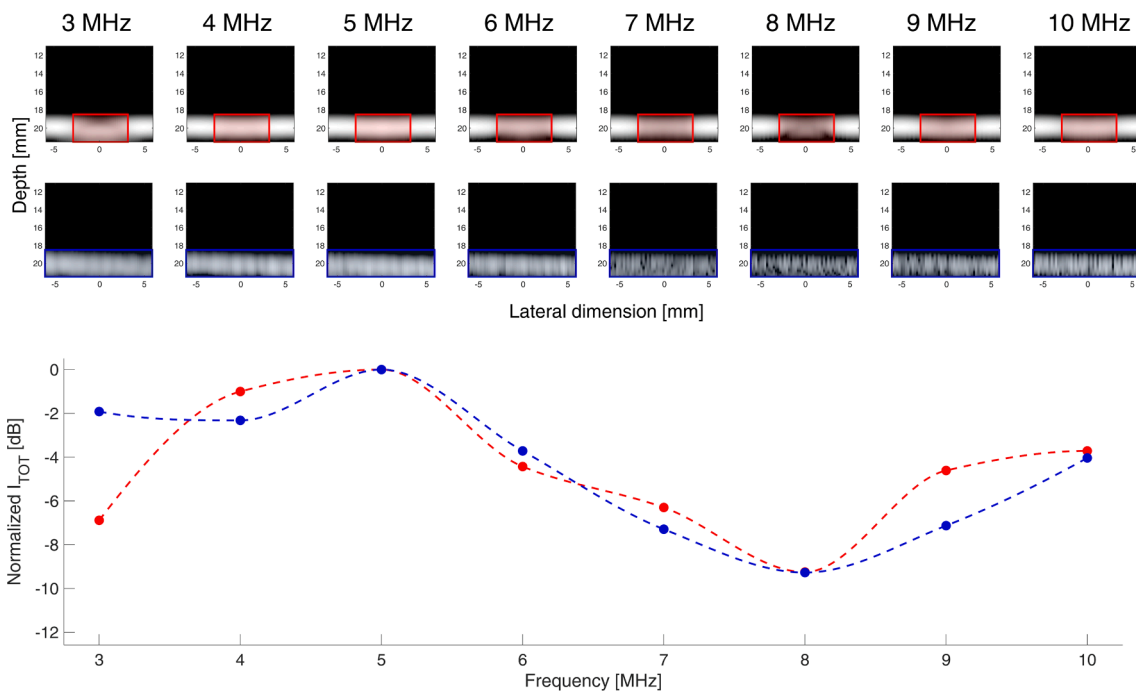

Fig. 5. Examples of reconstructed images (scatterers' diameter equal to 550 μm) are shown (top) together with the corresponding normalized I_{TOT} graph (bottom). The first row shows the reconstructed images for *in silico* experiments, whereas the second row shows the reconstructed images for *in vitro* experiments (images are displayed with a 35-dynamic range). The ROIs in which the corresponding normalized I_{TOT} was computed are highlighted with red (*in silico*) and blue (*in vitro*) rectangles. The corresponding normalized I_{TOT} values, plotted as a function of frequency, are shown with red (*in silico*) and blue (*in vitro*) points (bottom). For visualization purpose, we also show the corresponding interpolated values (dashed lines), obtained with a PCHIP (Piecewise Cubic Hermite Interpolating Polynomial) interpolation (*pchip* MATLAB function) applied along frequency (0.01-MHz step size). (For interpretation of the references to colour in this figure legend, the reader is referred to the web version of this article.)

with the probe displacement, guided by an automatic positioning system (GAMPT, Merseburg, Germany). We have defined the axis parallel to the phantom width as lateral direction, and the axis parallel to the phantom length as elevation direction (Fig. 4, left). The phantom was placed at 2 cm of depth from the probe (Fig. 4, top right).

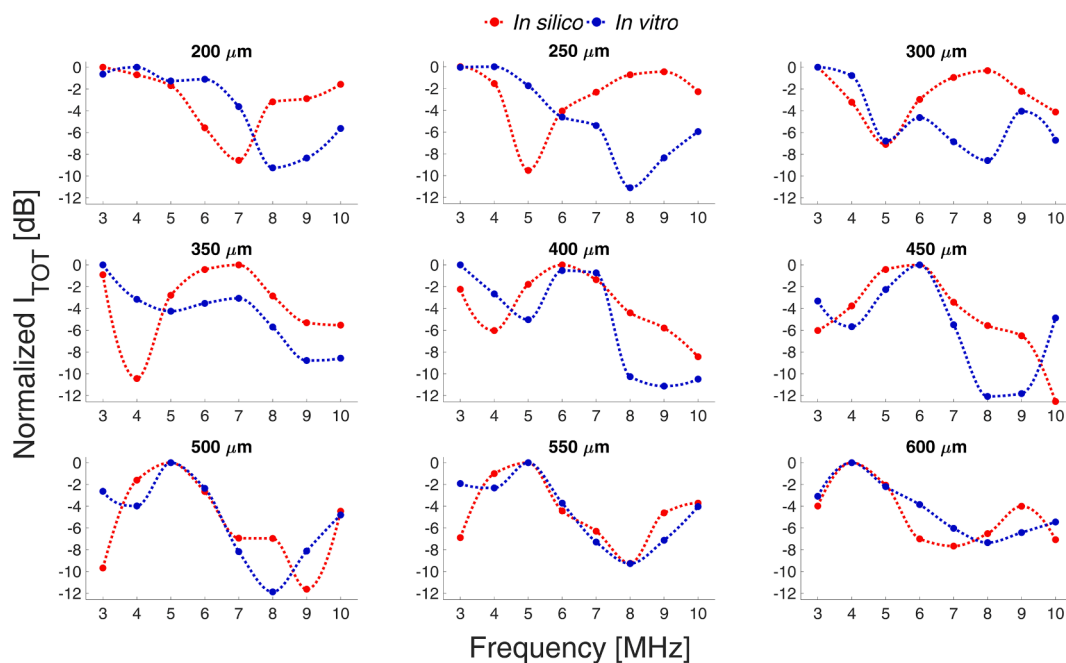The data were sequentially acquired. Specifically, the probe was

Fig. 6. The normalized I_{TOT} graphs (for each level of roughness) are shown. The normalized I_{TOT} values, plotted as a function of frequency, are shown with red (*in silico*) and blue (*in vitro*) points. For visualization purpose, we also show the corresponding interpolated values (dashed lines), obtained with a PCHIP (Piecewise Cubic Hermite Interpolating Polynomial) interpolation (*pchip* MATLAB function) applied along frequency (0.01-MHz step size). (For interpretation of the references to colour in this figure legend, the reader is referred to the web version of this article.)
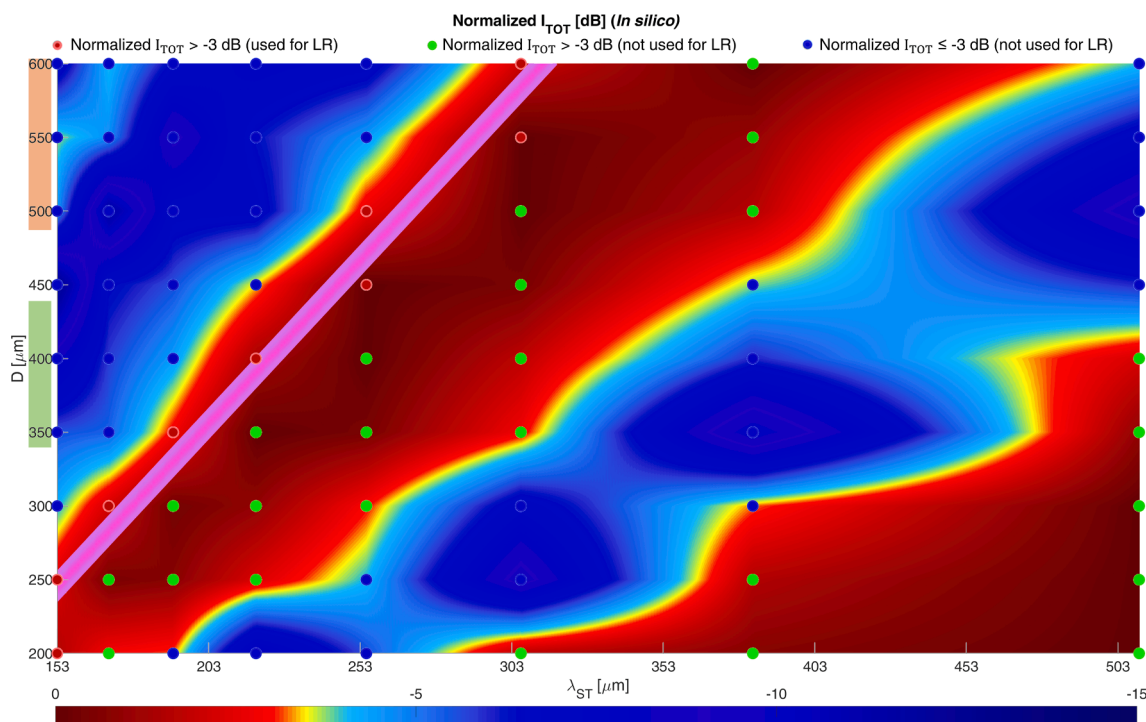

Fig. 7. The normalized I_{TOT} values for *in silico* experiments are shown as a function of λ_{ST} (*x-axis*) and semi-circular scatterers' diameter D (*y-axis*). The figure was generated by linearly interpolating the normalized I_{TOT} values along λ_{ST} (1-μm step size) and using the *pcolor* MATLAB function with interpolated shading. The figure is shown with a 15-dB dynamic range (colorbar at the bottom). Red points represent the values of normalized I_{TOT} > -3 dB used for LR (the obtained LR model is depicted in purple; the width and shadowing of the line representing the model were so defined to improve visualization). Green points represent the values of normalized I_{TOT} > -3 dB not used for LR, and blue points represent values of normalized I_{TOT} ≤ -3 dB (not used for LR). All these points (red, green, and blue) were obtained from Fig. 6 values (red points in each graph). The peripheral air-spaces dimensions generally observed in healthy subjects (between 340 and 440 μm) and in patients affected by COPD (above 490 μm) are highlighted along the *y-axis* in green and red, respectively. (For interpretation of the references to colour in this figure legend, the reader is referred to the web version of this article.)
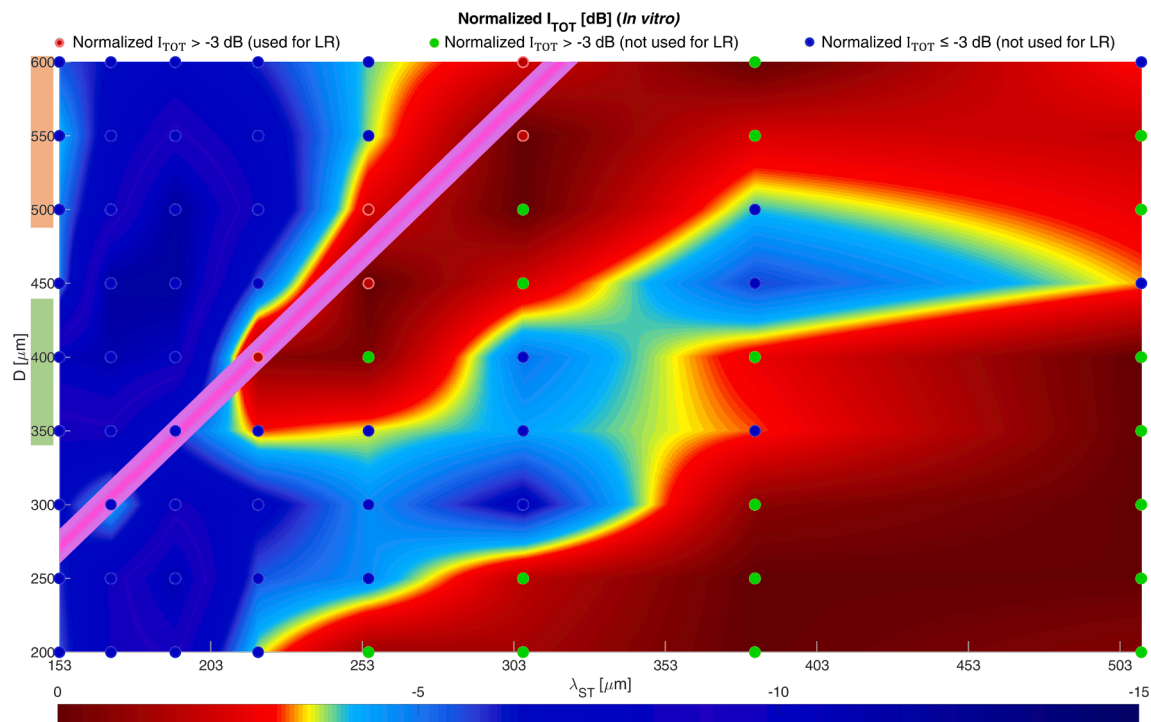
Fig. 8. The normalized I_{TOT} values for *in vitro* experiments are shown as a function of λ_{ST} (*x-axis*) and semi-circular scatterers' diameter D (*y-axis*). The figure was generated by linearly interpolating the normalized I_{TOT} values along λ_{ST} (1-μm step size) and using the *pcolor* MATLAB function with interpolated shading. The figure is shown with a 15-dB dynamic range (colorbar at the bottom). Red points represent the values of normalized $I_{TOT} > -3$ dB used for LR (the obtained LR model is depicted in purple; the width and shadowing of the line representing the model were so defined to improve visualization). Green points represent the values of normalized $I_{TOT} > -3$ dB not used for LR, and blue points represent values of normalized $I_{TOT} \leq -3$ dB (not used for LR). All these points (red, green, and blue) were obtained from Fig. 6 values (blue points in each graph). The peripheral air-spaces dimensions generally observed in healthy subjects (between 340 and 440 μm) and in patients affected by COPD (above 490 μm) are highlighted along the *y-axis* in green and red, respectively. (For interpretation of the references to colour in this figure legend, the reader is referred to the web version of this article.)

placed above the first rough stripe (Fig. 4, top right), and all the data corresponding to that roughness level were acquired with different center frequencies. Then, the probe was automatically moved along the elevation direction by 2 cm to acquire the data corresponding to the second roughness level. The process was repeated until reaching the last rough stripe.

2.2. Quantification of surface intensity

2.2.1. In silico

To estimate the surface intensity, a two-step procedure was applied to the reconstructed images. In step 1, to extract the envelope, the Hilbert transform was applied. Each reconstructed image was then normalized with respect to its maximum value. In step 2, we displayed the images in logarithmic scale with a 35-dB dynamic range, and defined a region of interest (ROI) in which we computed the total intensity (I_{TOT}) [9,11,12]. This ROI was defined as the area where the roughness was introduced, i.e., between −3 and 3 mm in the lateral dimension, and extending in depth from 18.5 mm to 21.5 mm (see Fig. 5, first row). The depth range was set by considering the spatial length of the transmitted pulse, i.e., $\frac{4\ \mu s\ \times\ 1580\ m/s}{2} \cong$ 3 mm, and the surface depth (20 mm). Only values above −35 dB in the ROI (empirical threshold) were used to compute I_{TOT} [9,11].

To evaluate the surface intensity as a function of frequency, we exploited a scaled version of I_{TOT} (normalized I_{TOT}). Specifically, for each roughness level, we normalized the eight I_{TOT} values (obtained with frequencies varying from 3 to 10 MHz) with respect to their maximum (see Fig. 5, bottom, red line) [9,11,12].

2.2.2. In vitro

The surface intensity was estimated *in vitro* with a procedure consistent with what was done *in silico*. The main differences are associated with step 1 and with the ROI definition. Specifically, as first operation, to be consistent with the *in silico* experiments, we evaluated only the 49 central lines (from approximately −6 to 6 mm along lateral dimension) of the reconstructed images. Considering only the central lines allowed us also to prevent undesired contributions coming from the edges of the steel phantom. Then, we applied a sixth-order bandpass Butterworth filter having a 1-MHz bandwidth and centered at the different center frequencies [12]. We successively applied the Hilbert transform to each filtered image, thus extracting the envelope [12]. To normalize the images consistently with what was done *in silico*, we acquired data from a smooth steel surface by using the same acquisition settings (e.g., from 3 to 10 MHz of center frequency and 0.5 MHz of bandwidth). Then, after having applied the same processing steps used for the rough surface (above mentioned), we extracted the 8 maximum values (one for each center frequency) from the smooth surface data. Finally, the rough surface images were normalized with respect to these maxima, and displayed in logarithmic scale with a 35-dynamic range. After these processing operations, the surface intensity was computed by means of the I_{TOT} parameter [9,11]. Specifically, this parameter was computed in a ROI extending over the entire lateral dimension (from approximately −6 to 6 mm) and depths from 18.5 mm to 21.5 mm (see Fig. 5, second row). The empirical threshold was set to −35 dB as done *in silico*.

The normalized I_{TOT} (see Fig. 5, bottom, blue line) was then computed as done *in silico*.
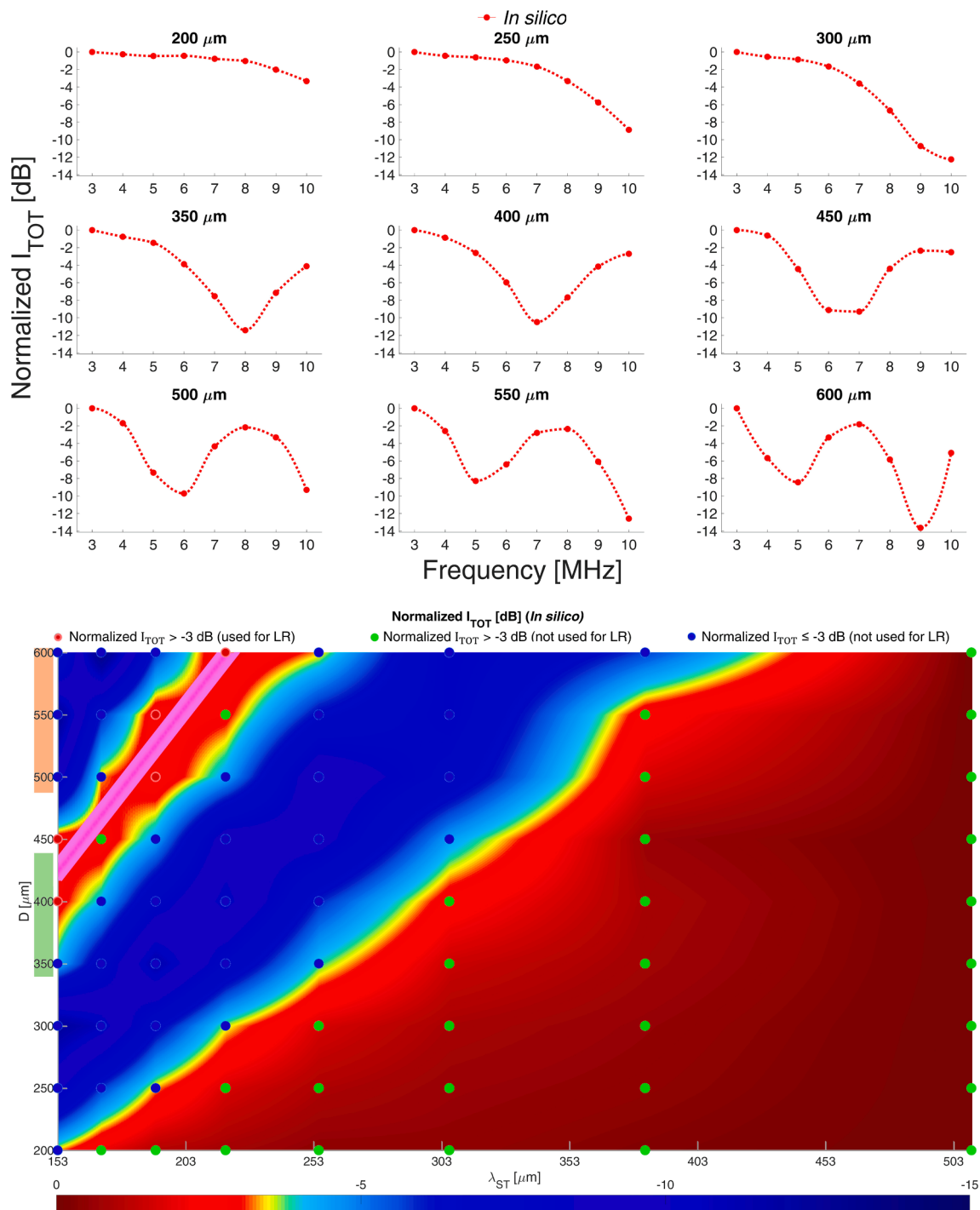
Fig. 9. The normalized I_{TOT} graphs (for each D) for *in silico* experiments with air are shown as a function of frequency (top). The normalized I_{TOT} values are shown with red points. For visualization purpose, we also show the corresponding interpolated values (red dashed lines), obtained with a PCHIP (Piecewise Cubic Hermite Interpolating Polynomial) interpolation (*pchip* MATLAB function) applied along frequency (0.01-MHz step size). At the bottom the normalized I_{TOT} values are shown as a function of λ_{ST} (*x-axis*) and D (*y-axis*). The figure was generated by linearly interpolating the normalized I_{TOT} values along λ_{ST} (1-µm step size) and using the *pcolor* MATLAB function with interpolated shading. The figure is shown with a 15-dB dynamic range (colorbar at the bottom). Red points represent the values of normalized $I_{TOT} > -3$ dB used for LR (the obtained LR model is depicted in purple; the width and shadowing of the line representing the model were so defined to improve visualization). Green points represent the values of normalized $I_{TOT} > -3$ dB not used for LR, and blue points represent values of normalized $I_{TOT} \leq -3$ dB (not used for LR). All these points (red, green, and blue) were obtained from the values depicted on top part of Fig. 9 (red points in each graph). The peripheral air-spaces dimensions generally observed in healthy subjects (between 340 and 440 µm) and in patients affected by COPD (above 490 µm) are highlighted along the *y-axis* in green and red, respectively. (For interpretation of the references to colour in this figure legend, the reader is referred to the web version of this article.)

3. Results

Fig. 6 shows the normalized I_{TOT} for the 9 different scatterers' diameter as a function of frequency for *in silico* (normalized I_{TOT}^{IS}; see Fig. 6, red graphs) and *in vitro* (normalized I_{TOT}^{IV}; see Fig. 6, blue graphs) experiments. It is observable how a strong agreement between normalized I_{TOT}^{IS} and normalized I_{TOT}^{IV} exists, and becomes stronger when the diameter increases.

To more precisely assess the consistency between *in silico* and *in vitro* results, Fig. 7 and Fig. 8 show the normalized I_{TOT} values for *in silico* (Fig. 7) and *in vitro* (Fig. 8) experiments as a function of λ and D. To consistently compare Fig. 7 and Fig. 8, we set in the *x-axis* the wavelength of soft-tissues (λ_{ST}), computed considering a speed of sound of 1530 m/s, which is between the speed of sound in water (1480 m/s; *in vitro* experiments) and in muscle (1580 m/s; *in silico* experiments). It is observable how the normalized I_{TOT} values seem to be consistent, and how it is possible to draw a linear model from both figures. Specifically, to model the relation between λ_{ST} and D, a linear regression (LR) model fitting specific normalized I_{TOT} values > -3 dB (red circles in Figs. 7 and 8) was obtained by means of the *fitlm* MATLAB function for both *in silico* (Fig. 7) and *in vitro* (Fig. 8) experiments. To further clarify, the −3-dB arbitrary threshold was applied to the normalized I_{TOT} values depicted in Fig. 6. Then, only a subgroup of values greater than −3 dB (red circles in Figs. 7 and 8) were used to fit the LR models depicted in Figs. 7 and 8 (purple line). Specifically, for each D (from 200 to 600 μm), we considered the first peak of normalized I_{TOT} (values greater than −3 dB) starting from the smallest λ_{ST} (highest frequency). However, for the *in vitro* experiments, the fit was performed by considering the peaks observed from 400 to 600 μm, as this approach seems not to work on these data for lower values of D (below 400 μm). The linear models obtained from *in silico* and *in vitro* experiments are D [μm] = −93.9794 + 2.2142 × λ_{ST} [μm] and D [μm] = −34.0824 + 1.992 × λ_{ST} [μm], respectively. By considering the *in vitro* results (Fig. 8), no peaks (values of normalized I_{TOT} > -3 dB) were observed for higher frequencies (8, 9 and 10 MHz) and, thus, smaller λ_{ST} (191, 170, and 153 μm). In contrast, *in silico* results showed peaks at those frequencies (Fig. 7). Overall, 34 (9 of which used for LR) and 24 (5 of which used for LR) peaks were detected *in silico* and *in vitro*, respectively.

Finally, we performed further numerical simulations following the same procedure adopted for steel but simulating air (speed of sound and volumetric mass density equal to 300 m/s and 1.23 kg/m³, respectively [13]) instead of steel. The results are shown in Fig. 9, where the obtained linear model is also presented (Fig. 9, bottom). The fit was performed by considering the peaks observed from 400 to 600 μm (as done for the experimental model made by steel), and the obtained linear model is D [μm] = 18.1648 + 2.6560 × λ_{ST} [μm]. The obtained linear model seems to be consistent with the model obtained in Fig. 7 (simulation of steel), with the main difference associated with a positive offset of about 112 μm.

4. Discussion and conclusions

LUS is an imaging modality used by clinicians to evaluate the state of the lung surface in real time [1,3]. However, LUS has a poor specificity as it is mainly based on the visual evaluation of imaging artifacts [1,2,4,5].

Even though recent attempts to develop LUS quantitative techniques exist [6–13], these approaches are applicable only to pathologies characterized by a reduction of air-spaces' dimensions [2,14]. Indeed, these techniques were developed to characterize a lung having an increased permeability with respect to ultrasound waves [2,14]. No quantitative approaches have been designed for lung pathologies characterized by an enlargement of air-spaces (impermeable lung) [14].

For this reason, in this article we have proposed a quantitative multifrequency approach to estimate the lung surface's roughness,

which can allow the indirect estimation of the air-spaces' dimensions [14]. This approach was tested both *in silico* and *in vitro* (using a novel experimental model).

As shown in Fig. 6, it is clear how by increasing D from 250 to 600 μm the variability between the *in silico* and *in vitro* results tends to decrease, especially for 550 and 600 μm. This can be explained by the ability of the steel model to consistently mimic the numerically simulated 2D domain when D is larger. Specifically, as shown in Fig. 3 and Fig. 4 (bottom right), micrometric imperfections in the printing process more strongly affect a roughness characterized by smaller values of D. Therefore, these imperfections could lead to stronger inconsistencies between *in silico* and *in vitro* results when D is smaller.

However, as the peripheral air-space dimensions are generally above 340 μm [17], the experimental model could be considered a reliable tool to mimic real air-spaces dimensions, which generate different roughness levels at the lung surface. Specifically, as above mentioned, the *in vitro* results are strongly consistent with *in silico* results for values of D above 500 μm, which correspond to the peripheral air-spaces dimensions of COPD patients [17]. This shows how this novel experimental model could be exploited to reliably mimic levels of roughness observable at the lung surface of patients affected by pathologies characterized by increased air-spaces' dimensions. Moreover, we have shown how a simple linear model could be utilized to assess surface roughness by measuring image intensity variations as a function of frequency.

Even though promising results were presented in this study, the presence of specific limitations should be highlighted. The first limitation consists in the presence of shear waves and mode conversions in steel, which were not considered *in silico*, but could potentially have played a role during the *in vitro* experiments. Moreover, contrary to what happens in steel (shear velocity equal to 3100 m/s [23]), shear waves should not play a significant role in lung tissue. Another limitation could be associated with the periodic and simplified geometry that we analyzed in this study with respect to a more heterogeneous geometry observable in real lungs. The small discrepancies between the imaging strategies utilized *in silico* and *in vitro* could also have an impact on the obtained results, even though both strategies are based on unfocused transmissions. In addition, it is important to highlight how the threshold to normalized I_{TOT} used to fit the linear models was arbitrarily set to −3 dB. Finally, even though the variation of intensities at the lung surface could be caused by different roughness levels, it could be caused also by other lung abnormalities, such as sub-pleural consolidations. All these aspects should be evaluated when translating this multifrequency approach *in vivo*.

In this study, for simplicity, only unfocused (plane wave) transmissions were employed. In future studies, the impact of focused beams will also be investigated. As other future studies, we aim at assessing how the presence of a heterogeneous medium in the first 20 mm of depth can impact on the roughness estimation. Moreover, the impact of the ultrasound beam's angle of incidence on the roughness estimation will be analyzed. After this, we also plan to validate this quantitative multifrequency approach *in vivo* by acquiring and analyzing RF data from COPD patients.

Declaration of Competing Interest

The authors declare that they have no known competing financial interests or personal relationships that could have appeared to influence the work reported in this paper.

Data availability

Data are available at the following link https://drive.google.com/drive/folders/1TA-VoHpShULrIr9Y4EnjRHo9QJ9tYZdp?usp=sharing.

Acknowledgments

References

[1] L. Demi, F. Wolfram, C. Klersy, A. De Silvestri, V.V. Ferretti, M. Muller, D. Miller, et al., New International Guidelines and Consensus on the Use of Lung Ultrasound, J. Ultrasound Med. 42 (2023) 309–344, https://doi.org/10.1002/jum.16088.

[2] F. Mento, U. Khan, F. Faita, A. Smargiassi, R. Inchingolo, T. Perrone, L. Demi, State of the Art in Lung Ultrasound, Shifting from Qualitative to Quantitative Analyses, Ultrasound Med. Biol. 48 (2022) 2398–2416, https://doi.org/10.1016/j.ultrasmedbio.2022.07.007.

[3] L. Demi, Lung ultrasound: The future ahead and the lessons learned from COVID-19, J. Acoust. Soc. Am. 148 (2020) 2146–2150, https://doi.org/10.1121/10.0002183.

[4] G. Soldati, M. Demi, A. Smargiassi, R. Inchingolo, L. Demi, The role of ultrasound lung artifacts in the diagnosis of respiratory diseases, Expert Rev. Respir. Med. 13 (2019) 163–172, https://doi.org/10.1080/17476348.2019.1565997.

[5] G. Soldati, M. Demi, R. Inchingolo, A. Smargiassi, L. Demi, On the Physical Basis of Pulmonary Sonographic Interstitial Syndrome, J. Ultrasound Med. 35 (2016) 2075–2086, https://doi.org/10.7863/ultra.15.08023.

[6] L. Demi, W. van Hoeve, R.J.G. van Sloun, G. Soldati, M. Demi, Determination of a potential quantitative measure of the state of the lung using lung ultrasound spectroscopy, Sci. Rep. 7 (2017) 12746, https://doi.org/10.1038/s41598-017-13078-9.

[7] X. Zhang, T. Osborn, B. Zhou, D. Meixner, R.R. Kinnick, B. Bartholmai, J. F. Greenleaf, et al., Lung Ultrasound Surface Wave Elastography: A Pilot Clinical Study, IEEE Trans. Ultrason. Ferroelectr. Freq. Control 64 (2017) 1298–1304, https://doi.org/10.1109/TUFFC.2017.2707981.

[8] K. Mohanty, J. Blackwell, T. Egan, M. Muller, Characterization of the Lung Parenchyma Using Ultrasound Multiple Scattering, Ultrasound Med. Biol. 43 (2017) 993–1003, https://doi.org/10.1016/j.ultrasmedbio.2017.01.011.

[9] F. Mento, G. Soldati, R. Prediletto, M. Demi, L. Demi, Quantitative Lung Ultrasound Spectroscopy Applied to the Diagnosis of Pulmonary Fibrosis: The First Clinical Study, IEEE Trans. Ultrason. Ferroelectr. Freq. Control 67 (2020) 2265–2273, https://doi.org/10.1109/TUFFC.2020.3012289.

[10] L. Demi, M. Demi, R. Prediletto, G. Soldati, Real-time multi-frequency ultrasound imaging for quantitative lung ultrasound – first clinical results, J. Acoust. Soc. Am. 148 (2020) 998–1006, https://doi.org/10.1121/10.0001723.

[11] F. Mento, L. Demi, On the Influence of Imaging Parameters on Lung Ultrasound B-line Artifacts, in vitro study, J. Acoust. Soc. Am. 148 (2020) 975–983, https://doi.org/10.1121/10.0001797.

[12] F. Mento, L. Demi, Dependence of lung ultrasound vertical artifacts on frequency, bandwidth, focus and angle of incidence: An in vitro study, J. Acoust. Soc. Am. 150 (2021) 4075–4082, https://doi.org/10.1121/10.0007482.

[13] E. Peschiera, F. Mento, L. Demi, Numerical study on lung ultrasound B-line formation as a function of imaging frequency and alveolar geometries, J. Acoust. Soc. Am. 149 (2021) 2304–2311, https://doi.org/10.1121/10.0003930.

[14] F. Mento, L. Demi, "Multi-Frequency Approach to Estimate the Roughness of Lung Surface, in silico Study," in: 2022 IEEE Int. Ultrason. Symp., 1–4. (**2022**). 10.1109/IUS54386.2022.9957410.

[15] World Health Organization (WHO) *Chronic obstructive pulmonary disease (COPD)*, Available: https://www.who.int/news-room/fact-sheets/detail/chronic-obstructive-pulmonary-disease-(copd), (date last viewed: 13-Apr-23). (**2023**). Retrieved April 13, 2023, from https://www.who.int/news-room/fact-sheets/detail/chronic-obstructive-pulmonary-disease-(copd).

[16] World Health Organization (WHO) *The top 10 causes of death*, Available: https://www.who.int/news-room/fact-sheets/detail/the-top-10-causes-of-death, (date last viewed: 13-Apr-23). (**2020**). Retrieved April 13, 2023, from https://www.who.int/news-room/fact-sheets/detail/the-top-10-causes-of-death.

[17] T. Beinert, P. Brand, J. Behr, C. Vogelmeier, J. Heyder, Peripheral Airspace Dimensions in Patients With COPD, Chest 108 (1995) 998–1003, https://doi.org/10.1378/chest.108.4.998.

[18] M. Takahashi, J. Fukuoka, N. Nitta, R. Takazakura, Y. Nagatani, Y. Murakami, H. Otani, et al., Imaging of pulmonary emphysema: a pictorial review, Int. J. Chron. Obstruct. Pulmon. Dis. 3 (2008) 193–204, https://doi.org/10.2147/copd.s2639.

[19] B.E. Treeby, B.T. Cox, k-Wave: MATLAB toolbox for the simulation and reconstruction of photoacoustic wave fields, J. Biomed. Opt. 15 (2010) 1–12. Retrieved from 10.1117/1.3360308.

[20] P. Tortoli, L. Bassi, E. Boni, A. Dallai, F. Guidi, S. Ricci, ULA-OP: An Advanced Open Platform for Ultrasound Research, IEEE Trans. Ultrason. Ferroelectr. Freq. Control 56 (2009) 2207–2216, https://doi.org/10.1109/TUFFC.2009.1303.

[21] L. Spicci, "FEM Simulation for 'Pulse-Echo' Performances of an Ultrasound Imaging Linear Probe," Proc. COMSOL 2013 Rotterdam, (**2013**).

[22] T.L. Szabo, Diagnostic Ultrasound Imaging: Inside Out, Diagnostic Ultrasound Imaging Insid. Out (2004), https://doi.org/10.1055/s-2005-861725.

[23] David R Lide *CRC Handbook of Chemistry and Physics, 84th Edition, 2003-2004*, Handb. Chem. Phys., (**2004**).